

DEVELOPMENT OF SI-BEARING 4TH GENERATION NI-BASE SINGLE CRYSTAL SUPERALLOYS

A.C. Yeh, K. Kawagishi, H. Harada, T. Yokokawa, Y. Koizumi, T. Kobayashi, D.H. Ping, J. Fujioka, T. Suzuki

High Temperature Materials Center, The National Institute for Materials Science (NIMS), 1-2-1 Sengen, Tsukuba Science City, Japan 305-0047

Keywords: 4th generation superalloys, Silicon addition, Ruthenium

Abstract

In present study, Si addition (1.0at%) is found to be responsible for a dramatic improvement in high temperature oxidation resistance of 4th generation superalloys; this might be attributed to an increase in Al activity induced by Si to promote the formation of protective Al₂O₃ layer and improved adhesion between the Al₂O₃ and the substrate due to the presence of Si. However, there are debits associated with Si addition in terms of reduction in both heat-treatment window and microstructure stability. The National Institute for Materials Science has developed two experimental Si-bearing 4th generation superalloys that exhibit an excellent balance of resistances against mechanical deformation and environmental attack; their temperature capability of both creep and oxidation properties have reached an average of +40°C over CMSX-4. Hence, the cost-performance of 4th generation superalloys can potentially be improved by addition of Si. The present article aims to quantify the properties of these experimental Si-bearing compositions in order to aid the future development of new superalloys with Si additions.

Introduction

For future jet engines to meet the ever-increasing demands of ecological compatibility, continuing research efforts have been focused on increasing the temperature capability of Ni-base single crystal superalloy, which is used as the turbine blade material, in order to cope with the incremental turbine entry temperature designed for improving the thermodynamic efficiency of gas turbine.

During the past decade, the addition of Ru has led to the development of 4th and 5th generation single crystal superalloys with improved creep strength [1,2]; the utilization of Ru can accommodate more refractory elements in the alloy system for strengthening without jeopardizing the microstructure stability [1,2]. However, there is drawback associated with oxidation resistance. Ru-bearing alloys can form RuO₄ during high temperature exposure; not only RuO₄ has high vapour pressure at high temperatures, but also can RuO₄ disrupt the formation of uniform Al₂O₃ layer and result in spallation of protective Al₂O₃ [3, 4]. In addition, high density and high cost of Ru are hindering the application of Ru-bearing superalloys. To improve the cost-performance of advanced superalloy that contains high amount of refractory elements, one must improve its resistance against

environmental degradation, e.g. oxidation. To achieve this, the National Institute for Materials Science (NIMS) has exploited Si addition in the system of the 4th generation superalloy, within the scope of a NIMS patent application [5].

Although Y&La addition can improve oxidation resistance of superalloy, they are difficult to be retained in the final product [6]; adding Si is more industrially viable in terms of controlling compositions in the final casting product. Furthermore, Si was already reported to have dramatic effect on improving the oxidation resistances of B-1900, IN713C, and Mar-M200 alloys [7]. However, a decrease in mechanical strength associated with Si addition was also reported [7]. The present article describes an attempt to improve the oxidation resistance of a 4th generation superalloy, while maintaining its excellent creep properties. The aim is to aid the realization of practical application for 4th generation superalloys.

Experiments

In this study, TMS-138A, a 4th generation superalloy with no Si content was used as the base alloy to derive two compositions; one had 1at% Si to substitute with 1at% Cr, and the other had 1at% Si to substitute with 1at% Mo. Chemical compositions are given in Table I; the rationales behind the chemistries of TMS-138A, and two Si-containing alloys are described here. The NIMS in-house alloy design program, which is constructed on a database of phase relationships and physical properties of over two hundred compositions, was utilized to design the base alloy, TMS-138A [8, 9], and also to ensure that alloy densities of derivative compositions were kept at the same range as those of commercial superalloys.

The effectiveness of Si to provide high temperature oxidation resistance in relation with Cr can be elucidated by comparing the results of TMS-138A and TMS-138A-Cr+Si. Comparisons between properties of TMS-138A and TMS-138A-Mo+Si can help to determine the trade-off between strength and oxidation resistance by reducing Mo and adding Si.

Performances of Ni-base single crystal superalloys are governed by various factors that are sensitive to slight chemical changes, such as formation and adhesion of protective Al₂O₃ layer during high temperature oxidation, γ' volume fraction, lattice misfit between γ/γ' , and phase stability. These parameters of each alloy

Table I. Chemical compositions of TMS-138A, TMS-138A-Cr+Si, TMS-138A-Mo+Si, Ni content balanced (at%).

alloys	Co	Cr	Mo	W	Al	Ta	Re	Ru	Hf	Si
TMS-138A	6.2	3.9	1.9	1.9	13.4	2.0	2.0	2.3	0.04	-
TMS-138A-Cr+Si	6.2	2.9	1.9	1.9	13.4	2.0	2.0	2.3	0.04	1.0
TMS-138A-Mo+Si	6.2	3.9	0.9	1.9	13.4	2.0	2.0	2.3	0.04	1.0

were studied and correlated to their creep and cyclic oxidation properties in present article.

Table II. Impurity levels in samples of each alloy in present study (analytical techniques, LECO: carbon and sulphur, OE: phosphorous).

Unit: ppm	TMS-138A	TMS-138A -Cr+Si	TMS-138A -Mo+Si	CMSX-4
carbon (C)	20	34	13	48
phosphorous (P)	9	20	20	9
sulphur (S)	1	6	8	3

In addition, partitioning characteristic of Si between γ and γ' was determined by atom probe microanalysis and strain-ageing technique [10] coupled with scanning electron microscope observation (JEOL-JSM6060 SEM) and electron probe microanalysis (SHIMADZU EPMA-1610).

Single crystal samples used for experiments were vacuum induction melted and fabricated inside NIMS using standard directional solidification casting procedures; materials were supplied as 10mm diameter cylindrical bars with orientations within 10 degrees of the [001] orientation. Impurity levels in samples of each alloy are summarized in Table II. Experimental procedures are described in the following:

Heat Treatment Processes

A SETARAM SETSYS-24 differential thermal analyzer (DTA) was used to determine the liquidus, solidus, γ' solvus, so that heat-treatment trials could be conducted to establish the solution heat-treatment window. DTA result indicated that both Si-containing alloys exhibited narrower windows for heat-treatment than that of TMS-138A, but comparable to that of CMSX-4, Table III.

Samples of TMS-138A, TMS-138A-Cr+Si and TMS-138A-Mo+Si were subjected to solution treatment at peak temperatures 1340°C/10hours, 1310°C/20hours, and 1320°C/20hours, respectively. Both TMS-138A-Cr+Si and TMS-138A-Mo+Si required longer solution soak time to reduce the residual segregation of Re and W. The solution heat-treatment was followed by a primary ageing of 4hours at 1100°C and a secondary ageing of 16 hours at 870°C.

Table III. Differential thermal analysis results (heat treated samples).

Unit: (°C)	TMS-138A	TMS-138A -Cr+Si	TMS-138A -Mo+Si	CMSX-4
γ' Solvus	1277	1295	1290	1291
Solidus	1365	1334	1332	1337
Liquidus	1436	1425	1427	1404
h.t. Window	88	39	42	46

Creep Tests

Matching pairs of TMS-138A, TMS-138A-Cr+Si, and TMS-138A-Mo+Si with the same crystal orientations were chosen for

creep tests. Solution-treated and aged samples were machined into standard creep specimens and tested along the [001] direction to rupture under the following four conditions that are relevant to the actual creep conditions experienced by turbine blades during service: (1) 1100°C/137MPa, (2) 1000°C/245MPa, (3) 900°C/392MPa, and (4) 800°C/735MPa.

Cyclic Oxidation Tests

Specimen preparation involved electrical discharge machining (EDM) of samples into geometry of 9mmØ x 5mm; surfaces were finished with 600grade sandpaper polishing followed by cleaning with acetone. High temperature cyclic oxidation tests were conducted at 1100°C and 1150°C in air (1hour per cycle); specimen weight change was measured at the end of each cycle.

Lattice Misfit Measurements

A Rigaku Geigerflex ($\theta/2\theta$) vertical X-ray diffractometer was used to obtain characteristic γ'/γ peaks from as-solutioned samples. The hot stage of the diffractometer allows the scans to be performed at high temperatures (up to 1200°C) within a vacuum environment $\sim 1 \times 10^{-4}$ atm. Specimens were carefully machined into the specified dimensions and inserted into a Pt holder to minimize displacement error. The x-ray scans were collected with the anode generator set at 40kV and 200mA. Scans were performed at 1100°C for all alloys. Computer software was used to deconvolute the {002} superlattice reflection and determine peak position corresponding to γ and γ' . The lattice misfit was then determined for each alloy.

Determine elemental γ/γ' partitioning ratios

Two techniques were employed; the first was atom probe microanalysis. Square rods of approximately 0.2 mm x 0.2 mm x 10 mm were EDM cut out from single crystal bars of all alloys. These rods were then electropolished to sharp needle shape specimens for field ion microscopy (FIM) observation and three-dimensional atom probe (3DAP, Oxford nanoScience Ltd) analysis. FIM tips were prepared by electropolishing those square rods first in a solution of 10% perchloric acid with 90% ethanol at room temperature, and then applying micro-electropolishing using an electrolyte of 2% perchloric acid in butoxyethanol. Atom probe analyses were performed at tip temperatures of about 50 K under ultrahigh vacuum ($< 1 \times 10^{-8}$ Pa) with a pulse fraction (a ratio of pulse voltage to the static voltage) of 0.2 and a pulse repetition rate of 1500 Hz. Chemical profiles in both γ and γ' can be analyzed for the determination of partitioning ratios for elements.

The second method involved strain-ageing and EPMA analysis; the purpose was to determine the change in partitioning at elevated temperature, i.e. 1100°C. Samples were cold worked and annealed at 1240°C for 30hours. Under stress-annealing, the fine γ and γ' two-phase structures were coarsened by recrystallization, forming a coarse γ and γ' two-phase structure. In order to achieve equilibrium state at 1100°C, samples were cooled from 1240°C and then aged at 1100°C for 500hours, followed by water-quenching to freeze the microstructure for EPMA analysis. Due to the coarse structure of γ and γ' , EPMA could perform chemical analysis on both phases to determine partitioning ratio of each element quantitatively.

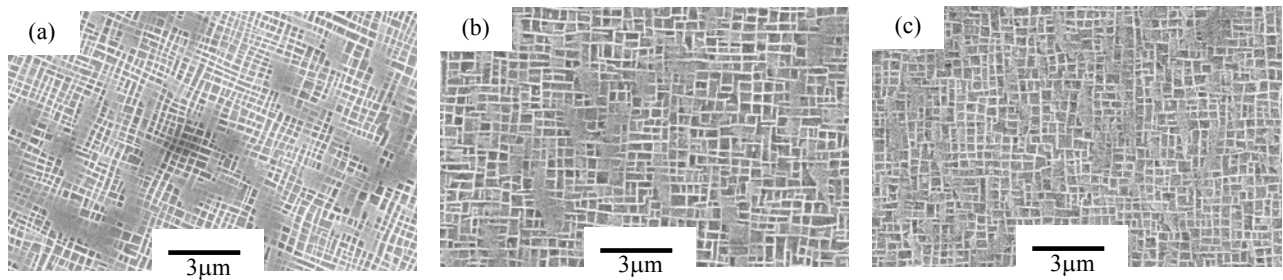


Figure 1. As heat treated microstructures, cuboidal γ' particles and γ matrix, (a) TMS-138A, (b) TMS-138A-Cr+Si, (c) TMS-138A-Mo+Si.

Results and Analysis

As heat-treated microstructures of TMS-138A, TMS-138A-Cr+Si and TMS-138A-Mo+Si were observed under SEM, Figure 1, images were then processed with image analyzer software to determine the volume fraction of γ' in each alloy. TMS-138A, TMS-138A-Cr+Si and TMS-138A-Mo+Si contain γ' volume fractions, 68%, 70% and 71%, respectively.

Creep Behaviours

Figure 2(a) shows the creep behaviours of all alloys under 800°C/735MPa. Both TMS-138A-Cr+Si and TMS-138A-Mo+Si exhibited significantly greater creep resistance than that of CMSX-4; creep rupture lives of CMSX-4, TMS-138A, TMS-138A-Cr+Si and TMS-138A-Mo+Si are 129hours, 1010hours, 1453hours and 1139hours, respectively. Both Si-bearing alloys outperformed their base alloy, TMS-138A.

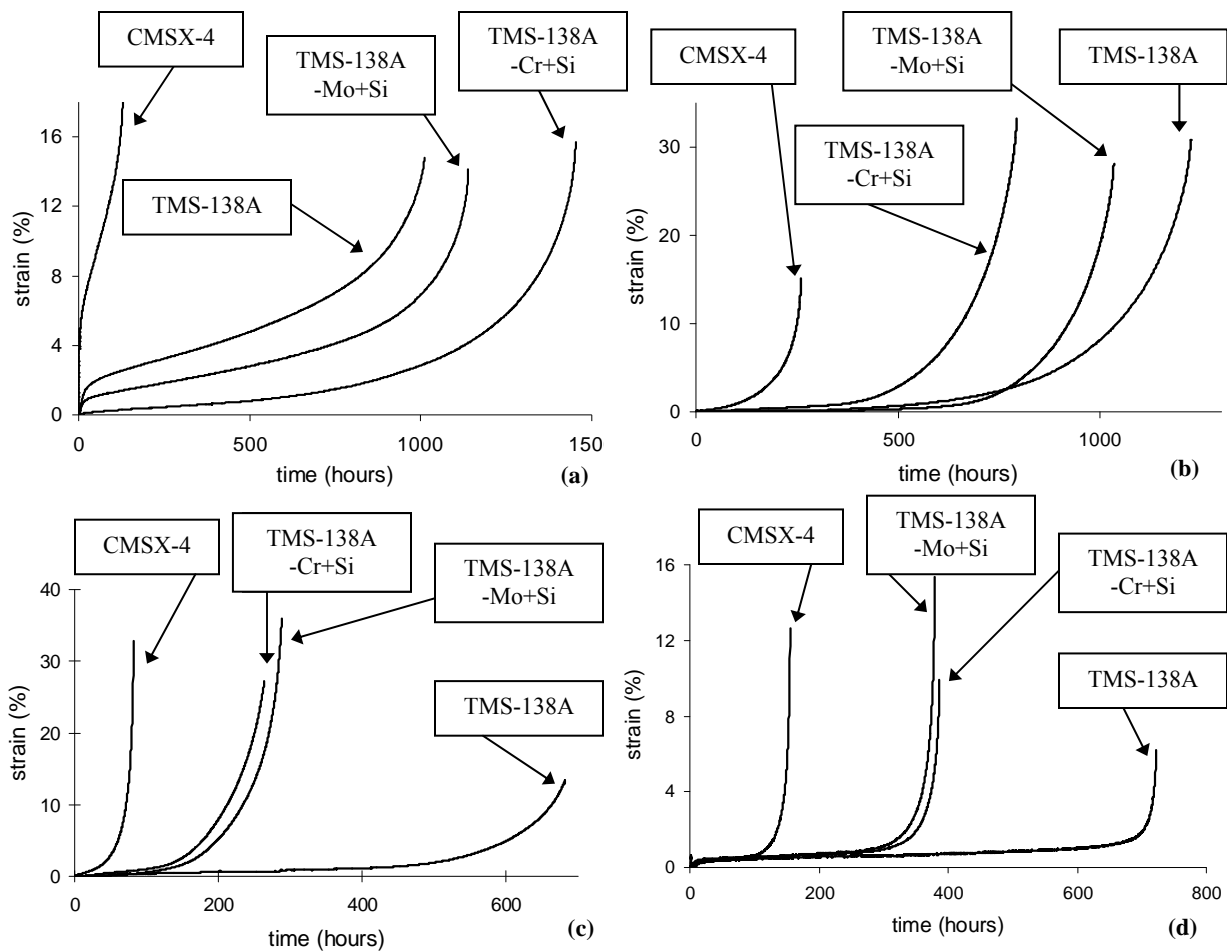


Figure 2. Creep curves (a) 800°C/735MPa, (b) 900°C/392MPa, (c) 1000°C/245MPa, (d) 1100°C/137MPa.

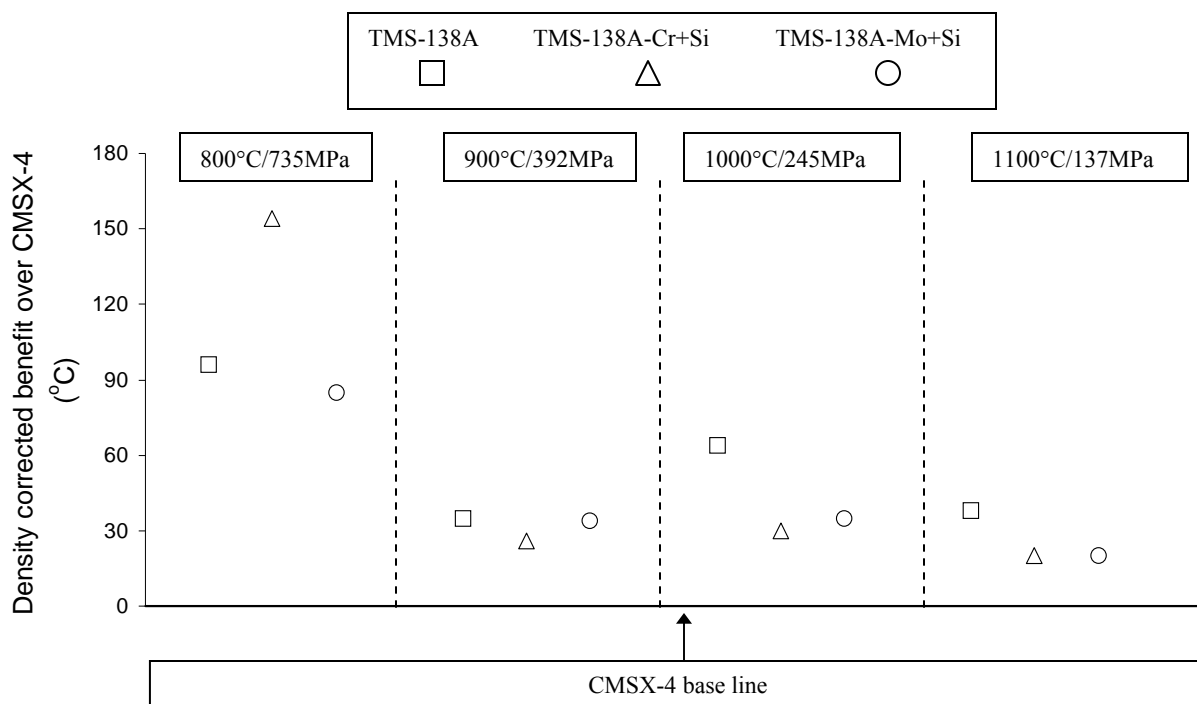


Figure 3. Density corrected 1% creep strain temperature benefit over CMSX-4 across 4 creep conditions.

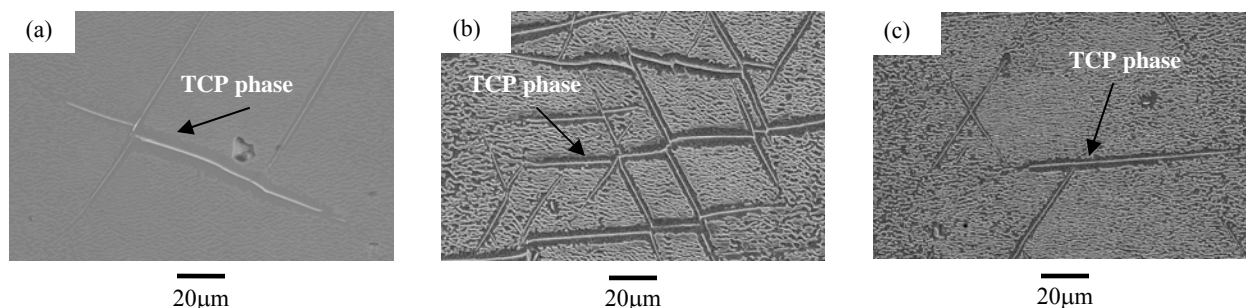


Figure 4. Microstructures of creep rupture samples under 1100°C/137MPa, (a) TMS-138A, (b) TMS-138A-Cr+Si, and (c) TMS-138A-Mo+Si

Creep curves under the condition of 900°C/392MPa are shown in Figure 2(b), TMS-138A performed slightly better than that of TMS-138A-Cr+Si, followed by TMS-138A-Mo+Si, then CMSX-4. TMS-138A exhibited an impressive creep rupture life of 1224hours; TMS-138A-Mo+Si and TMS-138A-Cr+Si crept to rupture after 1033hours and 793hours, respectively.

Contrary to previous creep results of Figure 2(a) and 2(b), both Si-bearing alloys significantly under-performed against TMS-138A under 1000°C/245MPa, Figure 2(c). TMS-138A-Cr+Si and TMS-138A-Mo+Si crept to rupture after 264hours and 288hours respectively; creep rupture life of TMS-138A was 682hours. Creep results of 1100°C/137MPa, Figure 2(d), have a similar trend as that of 1000°C/245MPa. Although both TMS-138A-Cr+Si and TMS-138A-Mo+Si were significantly more resistant than CMSX-4 against creep deformation, their base alloy, TMS-138A, performed the best; creep rupture lives of CMSX-4, TMS-138A, TMS-138A-Cr+Si and TMS-138A-Mo+Si were 155hours, 380hours, 387hours and 722hours, respectively.

To quantitatively compare the creep performances, temperature benefit of 1% creep strain (density corrected) of TMS-138A, TMS-138A-Cr+Si and TMS-138A-Mo+Si over CMSX-4 were determined by Larson-Miller estimation and plotted in Figure 3. It is clear that under all four creep conditions, TMS-138A, TMS-138A-Cr+Si and TMS-138A-Mo+Si outperformed CMSX-4 with an average of +40°C temperature benefit across the whole spectrum.

In summary, both Si-bearing alloys were the most creep resistance under 800°C/735MPa, especially TMS-138A-Cr+Si. All 4th generation alloys in present study performed similarly under 900°C/392MPa. Interestingly, under creep conditions of 1000°C/245MPa and 1100°C/137MPa, both Si-bearing alloys were not as strong as the base alloy against creep deformation. Creep rupture microstructures under 1100°C/137MPa are shown in Figure 4, TMS-138A-Cr+Si contained many topologically close packed (TCP) phases that can degrade creep resistance, Figure 4(b), comparing to TMS-138A, Figure 4(a).

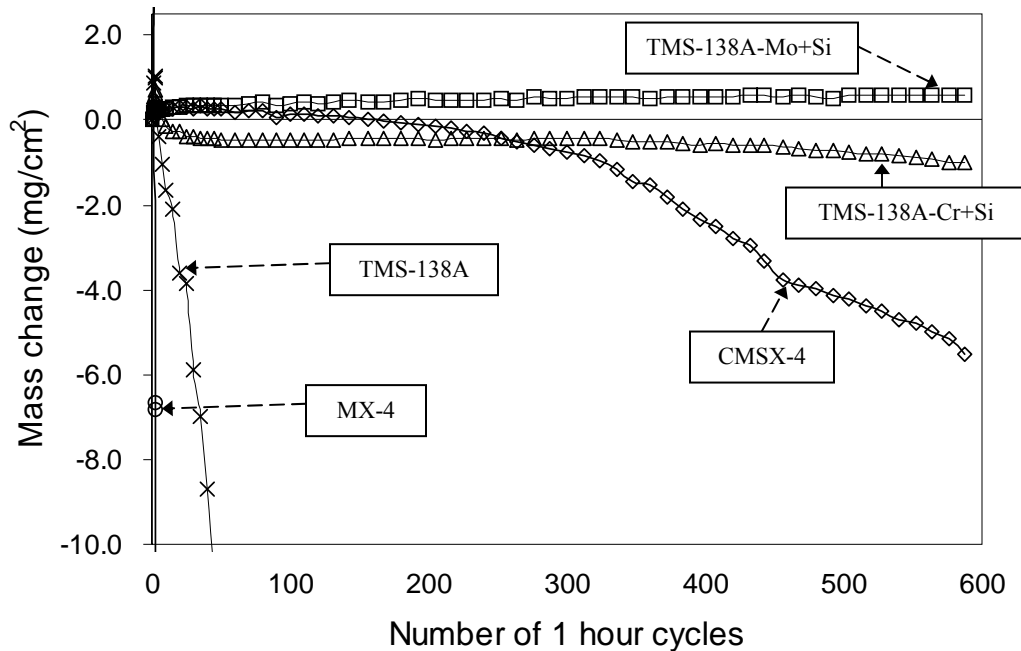


Figure 5. Cyclic oxidation tests (1100°C in air, 1hour/cycle). Oxidation resistance of TMS-138A-Cr+Si and TMS-138A-Mo+Si were significantly greater than that of TMS-138A and had surpassed that of CMSX-4.

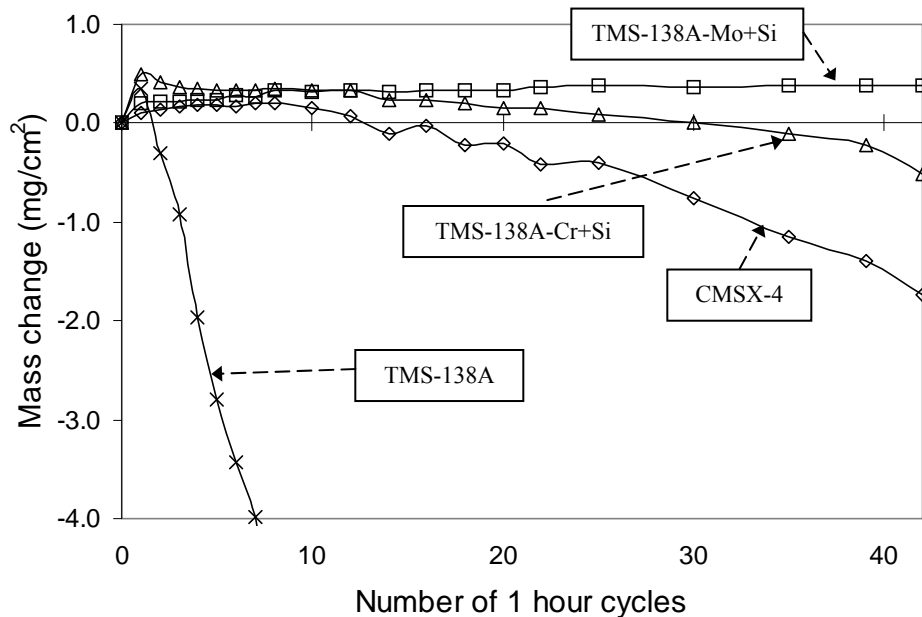


Figure 6. Cyclic oxidation tests (1150°C in air, 1hour/cycle). Oxidation resistance of TMS-138A-Cr+Si and TMS-138A-Mo+Si were significantly greater than that of TMS-138A and had surpassed that of CMSX-4.

Although TMS-138A-Cr+Si and TMS-138A-Mo+Si crept to rupture around 380hours, TMS-138A-Mo+Si was apparently more stable than TMS-138A-Cr+Si, i.e. TMS-138A-Mo+Si contains less amount of TCP phases.

Cyclic Oxidation in Air

Addition of 1.0at% Si has yielded remarkable improvement in oxidation resistance for TMS-138A-Cr+Si and TMS-138A-Mo+Si at 1100°C and 1150°C, Figure 5 and 6, respectively. At 1100°C, Figure 5, after 500 cycles, the oxidation resistances of

both Si-bearing alloys not only significantly surpassed that of their base alloy TMS-138A and an existing 4th generation superalloy MX-4, but also were shown to be superior to that of CMSX-4. Interestingly, TMS-138A-Mo+Si actually performed better than TMS-138A-Cr+Si. Figure 6, after 40 cycles at 1150°C, the oxidation resistance of TMS-138A-Mo+Si remained stable and was shown to be superior to that of TMS-138A-Cr+Si and CMSX-4, which was slowly dropping off. Again, the oxidation resistances of both TMS-138A-Cr+Si and TMS-138A-Mo+Si were far superior to that of their base alloy, TMS-138A. Actually, the resistance against oxidation at 1150°C of TMS-138A-Mo+Si coincides that of CMSX-4 at 1100°C when overlapping Figure 6 on Figure 5, hence, the Si-bearing alloy, TMS-138A-Mo+Si has achieved an improvement of +40°C benefit over CMSX-4 in terms of oxidation performance. Microstructure analysis, Figure 7, detected a continuous layer of Al₂O₃ underneath the NiO and spinel in both Si-containing alloys after 1 hour cyclic oxidation at 1100°C, Figure 7(c) and 7(d), by contrast, TMS-138A, did not form continuous Al₂O₃, Figure 7(a), this observation suggested that Si might have enhanced the Al activity attributing to the formation of continuous Al₂O₃ for good oxidation resistance, similar to that observed in CMSX-4, Figure 7(b). Referring back to Table II, all samples had very low and similar contents of C, S and P, so effects of impurity on oxide scale/substrate adhesion could be neglected. It is possible that Si addition may have improved the adhesion between the Al₂O₃ layer and the substrate, so that both Si-bearing alloys outperformed CMSX-4.

Si partitioning characteristic

Figure 8 illustrates a volume of analysis 7nm x 7nm x 25nm containing γ and γ' in TMS-138A-Mo+Si; the results of TMS-138A-Cr+Si is very similar. Figure 8(a) is the atom map of Al for referencing γ and γ' , and Figure 8(b) is the atom map of Si; Si was found to exhibit a slight preferential partitioning toward γ' with a partitioning ratio of $K_i=0.65$, where $K_i=C_{\gamma}(\text{composition in } \gamma)/C_{\gamma'}(\text{composition in } \gamma')$. This partitioning characteristic of Si may thus explain the increase in γ' volume fractions of both Si-containing alloys, Figure 1.

The partitioning characteristic of Si varies as the temperature increases to 1100°C, Figure 9. Si segregated in a manner similar to other γ' -formers; partitioning ratios of Si in TMS-138A-Cr+Si and TMS-138A-Mo+Si were 0.87 and 0.91, respectively.

There was no apparent effect on the partitioning characteristics of other elements by adding Si. For both Si-bearing alloys, Figure 9 shows that γ' phases were enriched with Al, Ta, while the solid solution strengthened FCC matrix contained characteristically elevated levels of Co, Cr, Re and Mo. W slightly partitioned toward γ . Ru was also observed to partition preferentially to the γ phase in a manner similar to Re, Cr and Co.

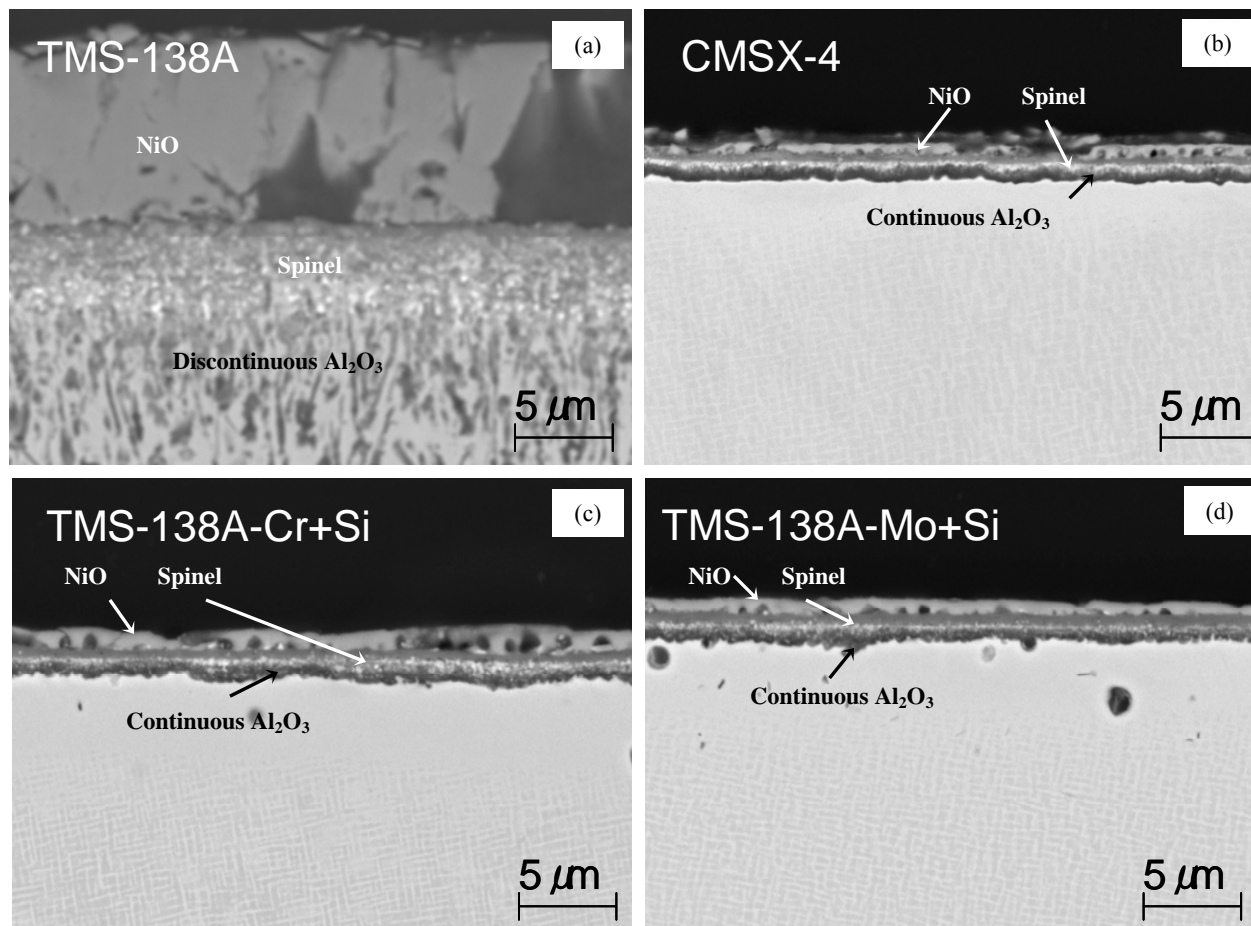


Figure 7. Microstructures after 1 hour cycle oxidation at 1100°C in air, (a) TMS-138A, (b) CMSX-4, (c) TMS-138A-Cr+Si and (d) TMS-138A-Mo+Si.

Although the partitioning coefficient of Si is ~ 0.65 , Figure 8, both TMS-138A-Cr+Si and TMS-138A-Mo+Si have higher volume fraction of γ' than TMS-138A to induce enrichment of refractory elements in the γ phase, such as Re and W, Figure 9. The direct substitution of Cr with Si and direct substitution of Mo with Si have significantly altered the lattice misfits of both Si-bearing superalloys, Figure 10. At 1100°C, TMS-138A-Cr+Si possessed slightly larger lattice misfit, $\delta=-0.41\%$, than TMS-138A, $\delta=-0.37\%$. And, the lattice misfit of TMS-138A-Mo+Si, $\delta=-0.32\%$, was smaller than that of the base alloy, TMS-138A.

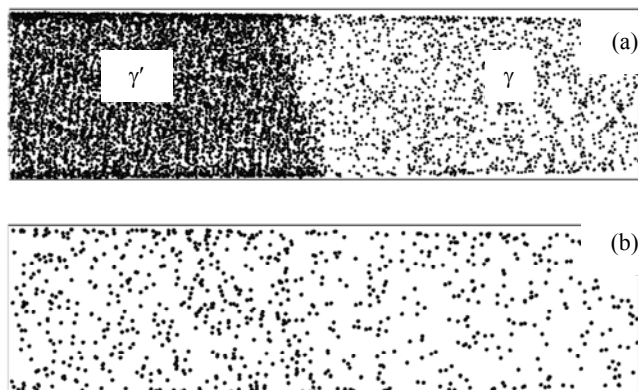


Figure 8. Atom probe microanalysis of a region (7nm x 7nm x 25nm) consists of γ and γ' , (a) Al atoms map, (b) Si atoms map. Si exhibits preferential partitioning to γ' , a $K_i (=C_{\gamma}/C_{\gamma'})$ value of 0.65; $i=\gamma/\gamma'$.

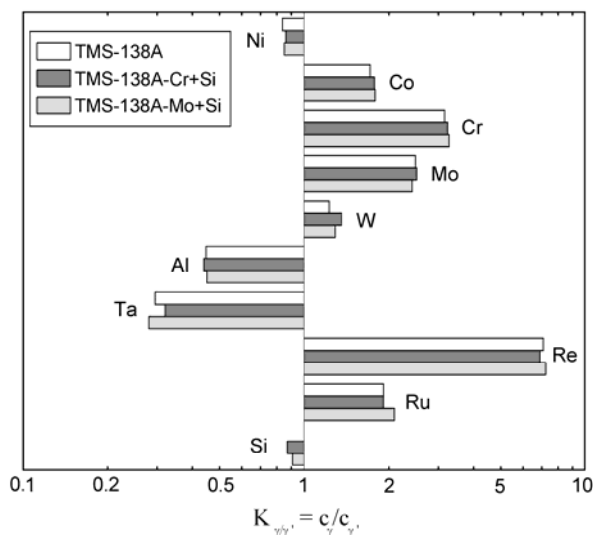


Figure 9. Elemental partitioning coefficients of two Si-bearing alloys in present study; experiments conducted at 1100°C. The 1100°C partitioning coefficient of Si became closer to unity. The K_i for Si in TMS-138A-Cr+Si and TMS-138A-Mo+Si were 0.87 and 0.91, respectively.

The purpose of this work is to design Si-bearing 4th generation superalloys that not only exhibit excellent creep strength but also impressive oxidation resistance. Experimental results indicate that both Si-bearing alloys developed have achieved +40°C benefits in both creep and oxidation resistances over CMSX-4; this is a breakthrough in the alloy development of single crystal superalloys. Typically, 4th generation superalloys contain high refractory alloying elements that are beneficial to improve the creep strength but harmful to the oxidation resistance; the two Si-bearing 4th generation superalloys in present article have performed beyond expectation owing to Si addition and smart composition adjustment with Cr and Mo by utilizing the NIMS alloy design programme.

The base alloy, TMS-138A, is a 4th generation superalloy, which has exhibited excellent creep strength and microstructure stability, Figure 2-4, however, its resistance against oxidation in bare condition is significantly less than that of CMSX-4, Figure 5 and 6. By substitution of 1.0wt% Cr with 1.0at% Si, TMS-138A-Cr+Si possesses impressive creep resistance at 800°C/735MPa, Figure 2(a), this can be attributed to an increase in γ' volume fraction. However, TMS-138A-Cr+Si appears to be prone to the formation of TCP phases that are detrimental to creep strength, Figure 4(c), due to the enrichment of TCP forming elements such as W and Re in γ phase, Figure 9. Hence the creep strength of TMS-138A-Cr+Si is not as good as TMS-138A under 1000°C and 1100°C creep conditions when microstructure stability is a critical factor for maintaining creep strength.

Most importantly, the oxidation resistance of TMS-138A-Cr+Si is better than that of CMSX-4, Figure 5 and 6. The presence of Si can promote the formation of protective Al_2O_3 , Figure 7(c), despite a reduced Cr content in the bulk composition. Hence the Al activity is likely increased by the presence of Si to form protective oxide during oxidation.

By substitution of 1.0at% Mo with 1.0at%Si, TMS-138A-Mo+Si behaves very differently from that of TMS-138A-Cr+Si. Mo is known to be a very effective solid solution strengthener and can increase the lattice misfit between γ and γ' [11]. However, Mo is detrimental to oxidation resistance and microstructure stability, because Mo-oxide is volatile and Mo is a TCP phase forming element [12]. Under creep condition at 800°C/735MPa, TMS-138A-Mo+Si outperforms TMS-138A owing to an increase in γ' volume fraction, however, the lower Mo content makes it underperformed against TMS-138A-Cr+Si, Figure 2(a). Although the microstructure stability of TMS-138A-Mo+Si is better than TMS-138A-Cr+Si, its creep resistance at 1100°C/137MPa is actually similar to that of TMS-138A-Cr+Si, Figure 4(d). This is due to the smaller lattice misfit in TMS-138A-Mo+Si, Figure 10, resulting lesser degree of interfacial strengthening when comparing to TMS-138A.

The oxidation resistance of TMS-138A-Mo+Si is the most impressive, not only has it significantly surpassed that of CMSX-4, but also has it reach +40°C benefit over CMSX-4, Figure 5 and 6. TMS-138A-Mo+Si is more resistant against oxidation and more stable against TCP formation than TMS-138A-Cr+Si owing to its higher Cr and lower Mo content, respectively.

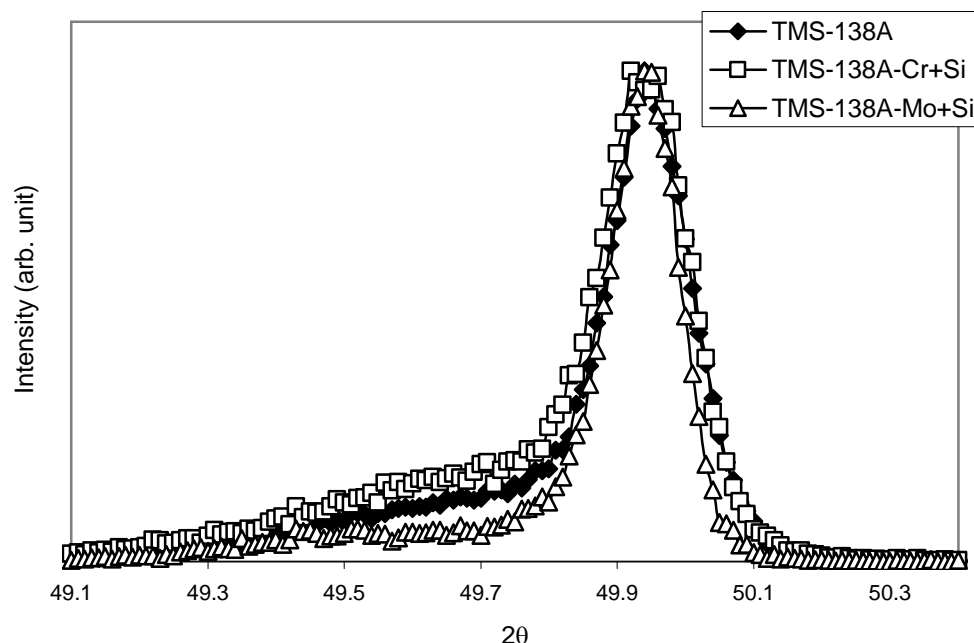


Figure 10. (200) peaks at 1100°C, the lattice misfits between γ and γ' for TMS-138A, TMS-138A-Cr+Si and TMS-138A-Mo+Si are measured to be -0.37%, -0.41% and -0.32%, respectively.

To confirm the effect of Si on Al activity, Thermo-Calc software has been used to calculate Al activities in five alloy systems, i.e. TMS-138A, TMS-138A-Cr, TMS-138A-Cr+Si, TMS-138A-Mo, and TMS-138A-Mo+Si. Results of calculation indicate that Si addition can dramatically increase Al activity, Figure 11. For example, Figure 11(a) shows that 1at% Cr reduction decreases the Al activity at 1150°C from 7.83E-08 to 6.05E-08 in TMS-138A-Cr, while 1at% Si addition can increase the Al activity from 6.05E-08 to 8.98E-08 in TMS-138A-Cr+Si. Al activity of TMS-138A decreases from 7.83E-08 to 6.24E-08 when Mo is reduced by 1at%; with 1at% Si addition, Al activity increases from 6.24E-08 to 9.45E-08 in TMS-138A-Mo+Si at 1150°C, Figure 11(b). TMS-138A-Mo+Si has the highest Al activity followed by TMS-138A-Cr+Si, then TMS-138A, Figure 11(c), which confirms the experimental observations in Figure 5 and 6.

Figure 7 shows that TMS-138A-Cr+Si, TMS-138A-Mo+Si and CMSX-4 have sufficient Al activity to form continuous Al_2O_3 after 1 hour exposure at 1100°C. Interestingly, TMS-138A-Cr+Si and TMS-138A-Mo+Si actually perform better than CMSX-4 against cyclic oxidation, Figure 5 and 6, so it is possible that adhesion between the protective Al_2O_3 layer and the substrate is improved due to Si addition. However, further work is required to confirm the effect of Si on the adhesion between Al_2O_3 /substrate.

Si addition in superalloys can increase the volume fraction of γ' ; this experimental observation is consistent with the partitioning characteristic of Si preferentially toward γ' and increased γ' solvus, Figure 8, 9 and Table II. Although the addition of Si might indirectly promote phase instability and reduce heat-treatment windows, the overall alloy chemistry can be optimized to compensate these debits. So, the cost-performance of high

refractory containing superalloys can be improved, like the two Si-bearing alloys developed by NIMS.

Conclusions

The present study has demonstrated unambiguously that Si is a promising alloying addition to further improve the 4th generation superalloys. Although the addition of Si promotes the risk of forming undesirable phases and lowering the incipient melting temperature, overall alloy chemistry can be optimised to minimise those negative effects of Si. The heat-treatment window, lattice misfit, γ' volume fraction and the degree of solid solution strengthening of an alloy system can be adjusted by overall alloy chemistry to accommodate Si addition, so Si-bearing Ni-base single crystal superalloys can be fabricable and exhibit good mechanical properties.

Experimental results and Thermo-Calc calculations have shown that Si addition can increase Al activity to promote the formation of protective Al_2O_3 layer during cyclic oxidation at 1100°C and 1150°C. The mechanism whereby addition of Si could improve the adherence of the protective Al_2O_3 is not quite clear and required further study.

Two experimental Si-containing 4th generation superalloys developed by NIMS not only have exhibited an excellent balanced creep and oxidation resistances, but also have their temperature benefits reached +40°C over CMSX-4. Hence the cost-performance of Ru-bearing superalloys can potentially be enhanced by adding Si, making the practical application of 4th generation superalloys closer to reality.

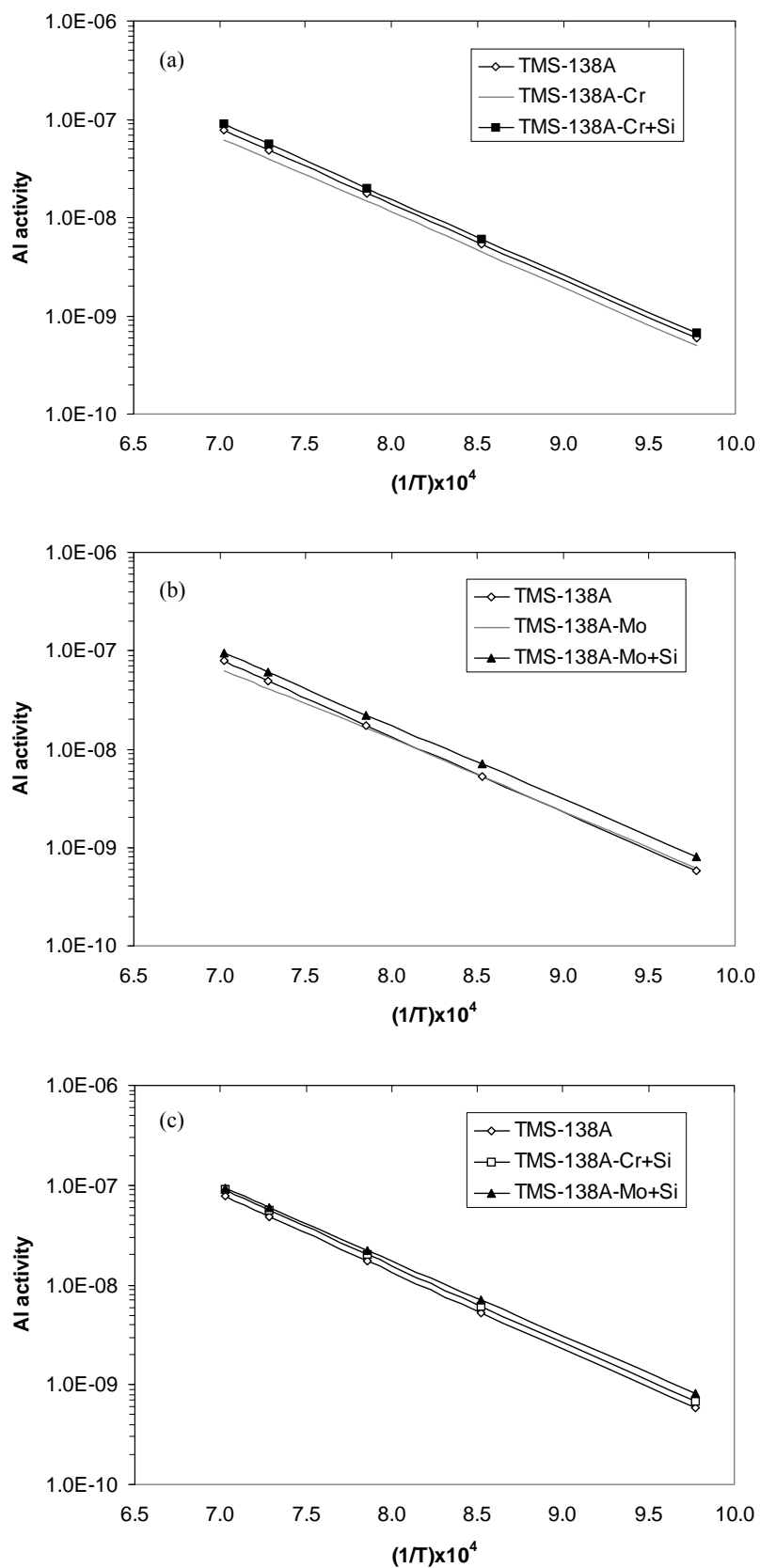


Figure 11. Al activity calculated by Thermo-Calc (a) TMS-138A vs TMS+138-Cr vs TMS-138A-Cr+Si, (b) TMS-138A vs TMS-138A-Mo vs TMS-138A-Mo+Si, (c) TMS-138A vs TMS-138A-Cr+Si vs TMS-138A-Mo+Si.

References

1. Zhang, J.X., Murakumo, T., Koizumi, Y., Kobayashi, T., Harada, H. and Masaki, S. JR. "Interfacial Dislocation Networks Strengthening a Forth-Generation Single-Crystal TMS-138 Superalloy", *Metallurgical and Materials Transactions A*, V33A, December (2002) pp.3741-3746.
2. Zhang, J.X., Koizumi, Y., Kobayashi, T., Murakumo, T., Harada, H. "Communications – Strengthening by γ/γ' Interfacial Dislocation Networks in TMS-162 – Toward a Fifth-Generation Single-Crystal Superalloy", *Metallurgical and Materials Transactions A*, V35A, June (2004) pp.1911-1914.
3. Kawagishi, K., Harada, H., Sato, A., Sato, A., Kobayashi, T., "The oxidation properties of forth generation single crystal superalloys" in the section of Research Summary, High temperature application of *JOM*, January 2006. pp. 43-46.
4. Kawagishi, K., Sato, A., Kobayashi, T., Harada, H. "Effects of alloying elements on the oxidation behaviour of 4th generation Ni-base single crystal superalloys", in issue 1 of Superalloys and Coatings for High Temperature Applications, volume 2, *TMS letters*, 2005. pp. 23-24.
5. Harada, H., Kawagishi, K., Kobayashi, T., Koizumi, Y., Sato, A., *Japan patent application 280993*, PCT patent application 319183.
6. Aimone, P.R., McCormick, R.L. "The effect of Yttrium and Sulfur on the Oxidation Resistance of an Advanced Single Crystal Nickel Based Superalloy", *Superalloys 1992*, edited by Antolovich, S.D. et al., the Minerals, Metals & Materials Society, Warrendale, Pa, USA, pp817-823.
7. Robert V. Miner, Jr. "Effects of Silicon on the Oxidation, Hot-Corrosion, and Mechanical Behaviour of Two Cast Nickel-Base Superalloys", *Metallurgical Transactions A*, Volume 8A, December 1977, pp1949-1954.
8. TMS-138/TMS-138A, NIMS forth generation single crystal superalloys, *NIMS brochure 2007*.
9. Yeh, A.C., Sato, A., Kobayashi, T., Harada, H. "On the Creep and Phase Stability of Advanced Ni-base Single Crystal Superalloys", *Materials Science and Engineering A*, (2008), doi: 10.1016/j.msea.2008.02.008.
10. Yokokawa, T., Osawa, M., Koizumi, Y., Kobayashi, T., Harada, H. "Estimation of γ/γ' Phase Equilibrium in Ru-bearing Ni-base Superalloys", *Journal of the Japan Institute of Metals* V68(8) August (2004) pp.577-581.
11. Zhang, J.X., Murakumo, T., Harada, H., Koizumi, Y., Kobayashi, T. "Creep deformation mechanisms in some modern single crystal superalloys", *Superalloys2004*, edited by Green, K.A. et al., the Minerals, Metals & Materials Society, Warrendale, Pa, USA, pp189-195.
12. Roger C. Reed, *The Superalloys Fundamentals and Applications*, (Cambridge, UK: Cambridge University Press, 2006), pp157-170.